

> REPLACE THIS LINE WITH YOUR MANUSCRIPT ID NUMBER (DOUBLE-CLICK HERE TO EDIT) <

Demonstration of inherently low differential phase noise across C-band in InP integrated, amplifying optical phased arrays

B.S. Vikram, M. Gagino, A. Millan-Mejia, L. Augustin, K.A. Williams, V. Dolores Calzadilla

Abstract— Optical phased arrays (OPAs) enable reliable and agile solid-state beam scanning for light detection and ranging (LiDAR), coherent beam combining, and free-space optical (FSO) communication systems. The performance of these systems strongly depends on the properties of the far-field pattern such as extinction ratio and side lobe suppression ratio, for maximizing the range and reliability of operation. Differential phase noise (DPN), a measure of the difference in time-varying phase fluctuations between the phased array channels, influences these characteristics, usually requiring the use of multiple phase-locked loops in fiber-based beam combining systems. In the present study, for the first time, we rigorously measure the differential phase noise between adjacent optical phased array channels integrated with phase modulators and in-line semiconductor optical amplifiers driven over a wide range of current densities in a generic InP photonic integrated platform. With the amplifiers driven at a current density of 5 kA/cm², the OPA channels generated an RMS differential phase noise of less than 10 mrad across the C-band, proving the capabilities of the InP photonic platform in inherently maintaining a high degree of temporal coherence between adjacent channels. The influence of the measured differential phase noise on the far-field pattern and the pointing error are analytically evaluated. The integrated platform's inherently low differential phase noise renders it suitable for implementing LiDAR and short-range FSO communication systems without active phase locking, significantly reducing system complexity.

Index Terms—differential phase noise, optical phased array, InP, semiconductor optical amplifier, active optical phased array

I. INTRODUCTION

Optical phased arrays (OPAs) [1], [2], [3] enable reliable and agile solid-state beam steering for free-space optical communications (FSO)[4], [5], light detection and ranging (LiDAR) [6], [7], and coherent beam combining systems [8], [9]. The OPA synthesizes a spatially structured far-field pattern composed of a prominent main lobe with the maximum power and progressively decaying sidelobes with deep nulls in between. The system range and reliability are maximized when the far-field pattern has a main lobe with the highest power, the narrowest width, the largest side lobe

suppression ratio (SLSR) [10], and the nulls have the highest extinction ratio.

OPA elements with optical amplifiers and phase modulators allow individual control of amplitude and phase realizing superior tailoring of the far-field pattern compared to purely phase control-based OPAs. This allows adaptive ranging in LiDAR applications. However, phase noise induced from path length fluctuations and amplifier noise temporally decorrelates the signals in the channels of the OPA. The difference in time-varying phase fluctuations between the channels of the phased array, characterized as differential phase noise (DPN) degrades the beam pattern by reducing the SLSR and the extinction ratio of nulls [11]. The DPN originates from temporally varying differences in path length [12] and noise from the optical amplifiers [13], [14] in the channels of the OPA.

The relative phase fluctuations between signal sources can be controlled with optical phase-locked loops (OPLLs) [15], [16]. Conventionally, in fiber-based systems, the DPN is suppressed with multilevel phase locked loops [12] for locking the array elements with individual fiber amplifiers in a coherent beam combining system. In this system, N-1 OPLLs are needed for an N-element OPA with one element as a reference. The linear scaling of the number of OPLLs with the array elements significantly increases implementational and operational complexity, leading to limitations on the scaling of number of OPA elements and consequently on system performance.

Photonic integration is expected to reduce the path length fluctuations over the fiber-based OPAs in addition to realizing significant gains in size, weight, power and cost (SWaP-C). Integrated OPAs have been demonstrated in various photonic platforms [1], [17] such as silicon (Si) [18], [19], indium phosphide (InP) [20], [21], and silicon nitride (SiN) [22], [23]. Among these platforms, InP provides an established fabrication platform [24], [25], [26] for implementing active OPAs with elements such as semiconductor optical amplifiers (SOAs) and phase modulators for amplitude and phase control. Phase noise (temporal phase fluctuations) induced through carrier density

This work has received funding support from the European Union Horizon 2020 program through the NewControl project under grant no 826653.

B.S. Vikram, M. Gagino, K.A. Williams and V. Dolores Calzadilla are with the Department of Electrical Engineering and the Eindhoven Hendrik Casimir Institute, Eindhoven University of Technology, Groene Loper 19, 5612 AP Eindhoven, The Netherlands (email: s.v.bhagavatula@tue.nl, m.gagino@tue.nl, K.A.Williams@tue.nl, V.Calzadilla@tue.nl).

A. Millan-Mejia and L. Augustin are with SMART Photonics, High Tech Campus 29, AE Eindhoven, The Netherlands (e-mail: alonso.millan-mejia@smartphotonics.nl, luc.augustin@smartphotonics.nl).

V. Dolores Calzadilla is also with Photonic Integration Technology Center, Groene Loper 19, 5612 AP Eindhoven, The Netherlands (e-mail: V.Calzadilla@tue.nl).

> REPLACE THIS LINE WITH YOUR MANUSCRIPT ID NUMBER (DOUBLE-CLICK HERE TO EDIT) <

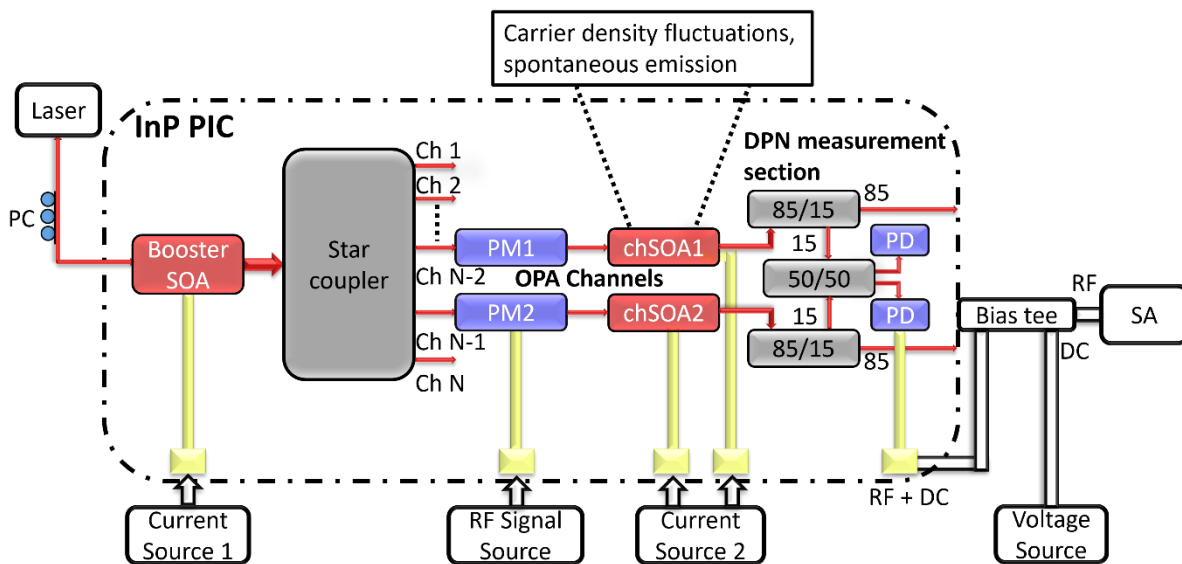


Fig. 1. Schematic of the setup showing the sections of the chip utilized for differential phase noise measurements. SOA-semiconductor optical amplifier, chSOA-channel semiconductor optical amplifier, 85/15, 50/50- multimode interference coupler split ratio, PM-phase modulator, SA-spectrum analyzer, PD-photodiode, PC-polarization controller, DPN-differential phase noise. Current Source 1: Keithley 2602B, Current Source 2: Thorlabs LDC 8005, Voltage Source: Keithley 2602B, RF Signal Source: Agilent 33220A.

fluctuations and amplified spontaneous emission (ASE) from the SOAs [14], along with path length fluctuations determines the extent of phase correlation among the OPA channels. The DPN between the integrated, amplifying OPA channels decides the PLL requirements. However, there have been no prior measurements of DPN in integrated OPAs.

In the present work, we perform the first measurements, to the best of our knowledge, of DPN between adjacent channels of photonic integrated circuit (PIC) based amplifying InP OPA driven over a wide range of current densities. The monolithically integrated OPA has an on-chip measurement structure composed of an MMI-based interferometer and photodetectors to enable DPN measurements. The measured RMS DPN (also referred to as RMS phase error) across the C-band is less than 10 mrad (in 100 Hz to 1 MHz frequency offset without any PLLs, amplifiers driven at 5 kA/cm²). In comparison, for conventional fiber-based systems [27], [28], active phase locking with OPLLs is required to reduce the RMS DPN to a few milliradians (8.2 mrad in 0.1 Hz to 6 kHz frequency offset with PLLs in [27], 314.2 mrad with PLL in [28]). The influence of DPN on the far-field beam pattern and the pointing error is analytically evaluated.

II. EXPERIMENTAL SETUP

Fig. 1 shows the setup schematic with sections of the InP photonic integrated circuit (PIC) (integrated OPA along with measurement structures) fabricated in the foundry platform of SMART photonics on an n-doped substrate (all the devices share a common ground contact). The on-chip measurement improves portability and allows the DPN measurements to be performed in real-world scenarios with varying operational conditions. The diagnostic data from the deployed chip would

improve the accuracy of estimated performance in different cases and is expected to drive design cycle improvements for the next generation of chips. Further, the DPN measurement structure also enables OPA calibration [29]. The OPA chip is operated at 18 °C (SOA performance was previously measured at this temperature [30]) and is pumped by an external laser with narrow linewidth (Keysight 81960A +14 dBm, 100 kHz). The optical polarization is aligned to the chip by adjusting the polarization controller to maximize the photocurrent of the reverse-biased booster SOA (2 mm long, 2 μm wide). Post alignment, the booster SOA is operated in the forward bias to provide gain. The amplified TE polarized signal is split by a star coupler to feed the individual OPA channels, each with a phase modulator (2.2 mm long) and a channel SOA (1 mm long, 2 μm wide).

The DPN measurements are performed by driving the booster (Keithley 2602B) and the channel SOAs (Thorlabs LDC 8005) at various current densities and utilizing an on-chip measurement structure that samples light from each adjacent OPA arm through multimode interference (MMI) couplers before mixing and beating them on the on-chip photodetectors (PDs).

A two-sided beat signal spectrum is needed to measure frequencies close to the carrier. To achieve this, the signal on one of the arms is frequency-shifted by applying a DC-shifted sinusoid to one of the phase modulators (frequency 3 MHz). While the DPN can be extracted from one of the heterodyne beat signals generated from the synthesized harmonics, the phase noise of the synthesized harmonic scales with the order (nth harmonic has n-times the phase noise of the signal source) [31]. However, the RF signal source utilized has low phase noise (Agilent 33220A has a specified typical phase noise of

> REPLACE THIS LINE WITH YOUR MANUSCRIPT ID NUMBER (DOUBLE-CLICK HERE TO EDIT) <

-115 dBc/Hz at 10 kHz offset).

Cross-talk is observed at the beat generated from the first harmonic (equal to the driving sinusoid frequency) due to the common ground contact for all the devices on the chip. The beat generated with the second harmonic (carrier shifted by 6 MHz) is selected for the measurement to have a strong signal-to-noise ratio without cross-talk while minimizing the influence of additional phase noise from the RF signal source. The DC bias of the phase modulator controls the fraction of optical power coupled to each photodetector and is optimized to increase the photocurrent of the detector from which the signal is extracted to maximize the signal-to-noise ratio (SNR). The purpose of optimizing the SNR is to ensure the measured DPN spectrum does not overlap with the noise floor (particularly at high frequencies), leading to inaccurate measurements. Variations in the carrier power (and thus the SNR) that do not overlap the DPN spectrum with the noise floor will not change the DPN as it is measured relative to the carrier power. The heterodyne beat signal is AC coupled to the spectrum analyzer (Agilent E4448A) through a bias tee that also sets the operating point of the photodiode (-2V DC bias) to control the responsivity and, thus, the generated photocurrent. The DPN is analyzed using the phase noise measurement (option 226) in the spectrum analyzer.

III. SYSTEM MODELING AND MEASUREMENT PRINCIPLE

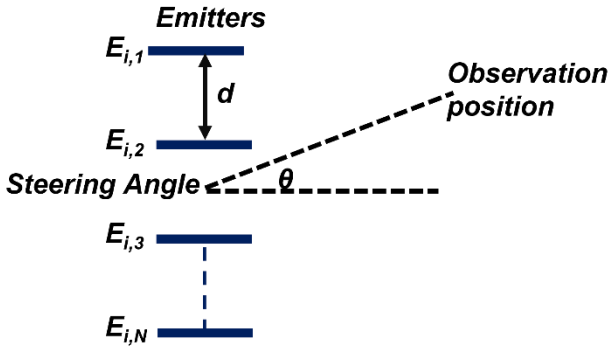


Fig. 2. Optical phased array with N emitters.

Fig. 2 shows an N-channel OPA with the electric field in each emitter channel and in the far-field described by (1-3)[32].

$$E_{i,n} = A_n \exp [j(\omega t + \phi_1 - (n-1)\Delta\phi + \phi_n(t))] \quad (1)$$

$$E_{o,n} = E_{i,n} \exp (-jk(n-1)dsin\theta) \quad (2)$$

$$E_t = \sum_{n=1}^N E_{o,n} \quad (3)$$

$E_{i,n}$ is the electric field from the n^{th} emitter, A_n is the amplitude of the n^{th} channel, ω is the angular frequency, t is the time, and $[\phi_1 - (n-1)\Delta\phi]$ is the phase of the n^{th} emitter. $\phi_n(t)$ represents the temporal phase fluctuations of the n^{th} emitter and consists of fluctuations from elements common to all emitters along with the fluctuations arising from the elements distinct to

each emitter. The objective of the present work is to measure and analyze the difference in temporal phase fluctuations between emitters, with the origin of the difference attributed to the distinct elements in each emitter (amplifier noise, path length fluctuations). Equations (2) and (3) describe the electric field at the observation point located at an angle θ . $E_{o,n}$ is the contribution to the electric field at the observation point in the far-field from the n^{th} emitter, d is the spacing between emitters, k is the wave vector and E_t is the total electric field. The signal propagation through the OPA and the on-chip measurement structure is described with equations to provide insights into the measurement principle.

$$E_{in} = E_{las} \exp (j(\omega_{opt} t + \phi_{laser}(t))) \quad (4)$$

$$E_{BSOA} = G_{BSOA} E_{in} \exp(j\phi_{BSOA}(t)) \exp(j\phi_{Bpath}(t)) \quad (5)$$

Equations (4) and (5) describe the signal upon propagation through the booster SOA. E_{las} , ω_{opt} , and $\phi_{laser}(t)$ are the amplitude, optical angular frequency, and temporal phase fluctuations (resulting in spectral domain phase noise) of the laser coupled to the chip. E_{in} , G_{BSOA} , and E_{BSOA} are the booster SOA's input electric field, gain, and output electric field respectively. $\phi_{BSOA}(t)$ and $\phi_{Bpath}(t)$ are the temporal phase fluctuations added to the signal in the booster SOA due to carrier density fluctuations and path length fluctuations (originating from thermal and vibrational effects occurring at various time scales). The amplified spontaneous emission (ASE) is not considered as the input signal strength is high, and the output of the booster SOA is saturated in the present case.

$$E_1 = k_1 E_{BSOA} \exp(j\phi_{path1}(t)) \quad (6)$$

$$E_2 = k_2 E_{BSOA} \exp(j\phi_{path2}(t)) \quad (7)$$

Equations (6) and (7) include the cascaded insertion loss and time-varying path length fluctuations in the two OPA channels between which the DPN is measured. The insertion loss in the two OPA channels is represented by k_1 and k_2 . $\phi_{path1}(t)$ and $\phi_{path2}(t)$ represent the path length originating temporal phase fluctuations in channels 1 and 2, respectively.

$$E_{PM2} = E_2 \exp (j(\frac{\pi V_{RF}}{V_\pi} \sin(\omega_{RF} t))) \quad (8)$$

$$E_{chSOA1} = G_{chSOA1} E_1 \exp(j\phi_{chSOA1}(t)) \quad (9)$$

$$E_{chSOA2} = G_{chSOA2} E_{PM2} \exp(j\phi_{chSOA2}(t)) \quad (10)$$

Equation (8) represents the phase modulation on one of the OPA channels with a sinusoid carrier of amplitude V_{RF} and angular frequency ω_{RF} (the phase noise of the RF signal source is low and is not considered here, V_π is the half-wave voltage of the phase modulator). Equations (9) and (10) add the gain and temporal phase fluctuations arising from carrier density fluctuations in channel SOAs 1 and 2 respectively.

> REPLACE THIS LINE WITH YOUR MANUSCRIPT ID NUMBER (DOUBLE-CLICK HERE TO EDIT) <

$$i_{PD} = R|k_{MMI1}E_{chSOA1} + k_{MMI2}E_{chSOA2}|^2 \quad (11)$$

$$i_{Bias\ tee\ RF} = Rk_{MMI1}k_{MMI2}[(E_{chSOA1})(E_{chSOA2}^*) + (E_{chSOA2})(E_{chSOA1}^*)] \quad (12)$$

$$i_{Bias\ tee\ RF} = K_{total} \cos[(\phi_{path1}(t) - \phi_{path2}(t)) + (\phi_{chSOA1}(t) - \phi_{chSOA2}(t)) + (\frac{\pi V_{RF}}{V_{\pi}}) \sin(\omega_{RF}t)] \quad (13)$$

Equation (11) describes the mixing of the signals sampled from the OPA channels with the MMI couplers to generate the beat signal. R is the responsivity of the photodetector, k_{MMI1} , and k_{MMI2} represent the amplitude factors with which signals are sampled from the two OPA channels.

Equation (12) describes the AC coupled signal at the RF port of the bias tee. Equation (13) details the terms contributing to the DPN and the frequency-shifted harmonics. $K_{total} = 2Rk_{MMI1}k_{MMI2}$. The first term inside the cosine is generated by the difference in the temporal path length fluctuations between the two OPA channels, while the second term is generated by the difference in the temporal phase fluctuations between the two channel SOAs. These two terms represent the differential phase noise. The third term describes the synthesized evenly spaced harmonics (spaced by $\omega_{RF}/2\pi$). Each harmonic is phase modulated by the DPN information. The common phase noise sourced from the laser, the booster SOA, and the path length fluctuations from the sections of the chip before the star coupler are canceled out. When the first two terms inside the cosine in (13) become zero, the temporal phase fluctuations in both the channels are identical (correlated) and the beat signal collapses to the driving sinusoid frequency. In contrast, the linewidth (phase noise) of the beat signal increases for the uncorrelated case.

IV. Results and Analysis

The measured DPN spectrum with the booster SOA and the channel SOAs driven at current densities of 5 kA/cm^2 is shown in Fig. 3 with the source laser operating at 1550 nm. The current density is defined as $J_{SOA} = I_{SOA} / (L_{SOA} W_{SOA})$, where I_{SOA} , L_{SOA} , and W_{SOA} are the injected current, length and width of the SOA respectively. The length of the channel SOAs is 1 mm and the length of the booster SOA is 2 mm, while the width of both types of SOAs is $2 \mu\text{m}$. For example, a current of 400 mA in the booster SOA would correspond to a current density of 10 kA/cm^2 . While the variation in the DPN can be expressed as a function of parameters such as the gain of the SOA and the output power, in the present case, it has been expressed as a function of current density, which is known with the highest accuracy.

The noise floor is measured by switching off the booster and the channel SOAs. When the temporal phase fluctuations between the two channels are identical, the DPN is zero, as the first two phase terms (inside the cosine) of equation 13 are zero.

In the case of strongly correlated phase fluctuations, the contribution from these terms will be minimal, and vice versa. Slow temporal phase fluctuations along the two-channel paths are strongly correlated and have a small contribution to the integrated DPN (area under the curve in different decades in Fig. 3) and vice-versa. The slope of the DPN climbs at a rate of $\sim 28 \text{ dB/decade}$ from 100 kHz to 10 kHz. The rapid climb is similar to the case where the temporal phase fluctuations between the two channels are weakly correlated. Between 10 kHz and 1 kHz, the growth of the DPN is arrested to $\sim 3 \text{ dB/decade}$ before flattening to $\sim 0.5 \text{ dB/decade}$ between 1 kHz and 100 Hz. This regime is similar to the case where the temporal phase fluctuations are strongly correlated. The measured DPN spectrum also presents similarities to the phase noise of the beat between lasers locked by an OPLL [16]. Even without an OPLL, the measured DPN is akin to the case where an OPLL with a loop bandwidth of nearly 10 kHz is implemented demonstrating that the DPN is inherently low in the InP amplifying, integrated OPA. The measurements are not performed at frequencies lower than 100 Hz as their contribution to the total DPN is predicted to be low as the slow frequency fluctuations in both the channels are expected to be strongly correlated in the two paths.

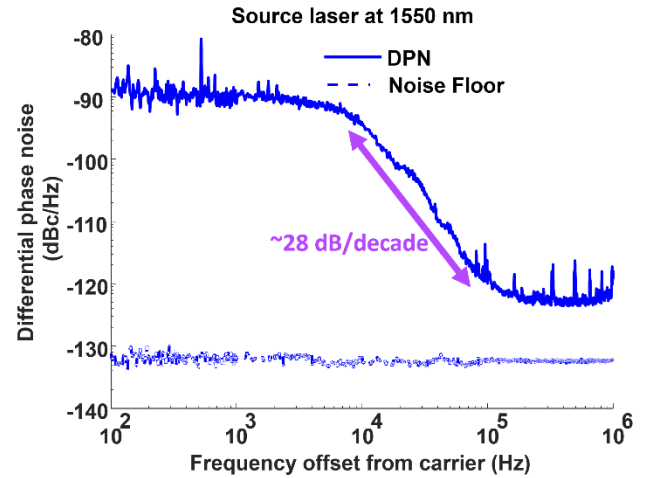


Fig. 3. Measured differential phase noise spectrum with the source laser at 1550 nm and measurement noise floor.

Fig. 4. shows the RMS DPN (obtained by integrating the DPN plot from 100 Hz to 1 MHz at $J_{BSOA} = J_{chSOA} = 5 \text{ kA/cm}^2$), which is less than 10 mrad across the C-band (corresponding to stability of $\lambda/628$). The variation in the measured DPN over five measurements is also shown, with the optical input re-aligned and the amplifiers toggled between on and off states in between the measurements. Each of the five measurements is averaged over 15 sweeps to improve the measurement accuracy.

Fig. 5 shows the mean values of the measured RMS DPN with the booster, and the channel SOA current densities varied between 5 kA/cm^2 to 10 kA/cm^2 (saturated regime) with the source laser at 1550 nm. At higher current densities, the output power drifts over time. This is the case for the following sets of current densities for the booster and the channel SOAs: ($J_{BSOA} = 7.5 \text{ kA/cm}^2$, $J_{chSOA} = 7.5 \text{ kA/cm}^2$), ($J_{BSOA} = 10 \text{ kA/cm}^2$,

> REPLACE THIS LINE WITH YOUR MANUSCRIPT ID NUMBER (DOUBLE-CLICK HERE TO EDIT) <

$J_{\text{chSOA}}=5 \text{ kA/cm}^2$), and ($J_{\text{BSOA}}=10 \text{ kA/cm}^2$, $J_{\text{chSOA}}=7.5 \text{ kA/cm}^2$). The drifts induce artifacts in the phase noise spectrum when averaged over several sweeps. The measurement instrument averages in each frequency decade before shifting to the next decade. As a result, discontinuities occur between different bands when the carrier power drifts during a measurement. To overcome this, the spectrum has to be obtained before the carrier power drifts. Reducing the averages from 15 to 5 achieves continuous spectra, albeit at the cost of increased uncertainty from each measurement. The uncertainty is partly alleviated by collecting multiple readings and averaging across them. Each measurement is divided into five sub-measurements, with each sub-measurement averaged over five sweeps. The average of the RMS DPN over these five sub-measurements constitutes a single measurement. The SOAs are not power-cycled among the sub-measurements that constitute a single measurement. The maximum DPN of 29 mrad (averaged over two measurements) occurs at $J_{\text{BSOA}}=10 \text{ kA/cm}^2$ and $J_{\text{chSOA}}=7.5 \text{ kA/cm}^2$.

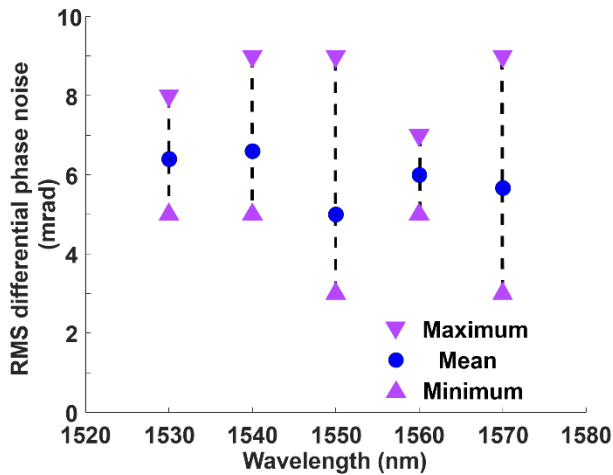


Fig. 4. Measured RMS differential phase noise in the C-band at $J_{\text{BSOA}}=J_{\text{chSOA}}=5 \text{ kA/cm}^2$.

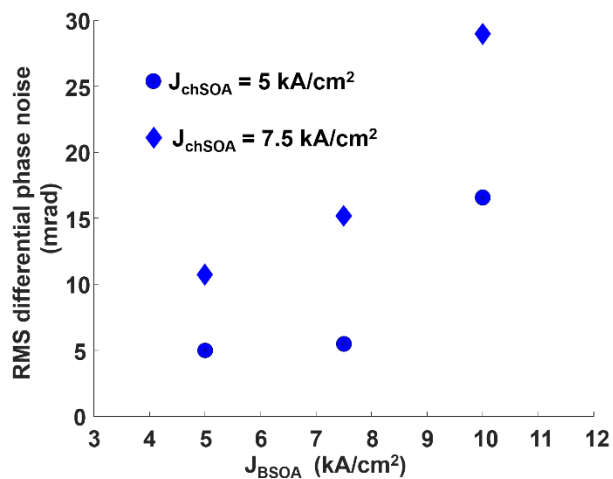


Fig. 5. Measured RMS differential phase noise at different booster (J_{BSOA}) and channel SOA (J_{chSOA}) current densities.

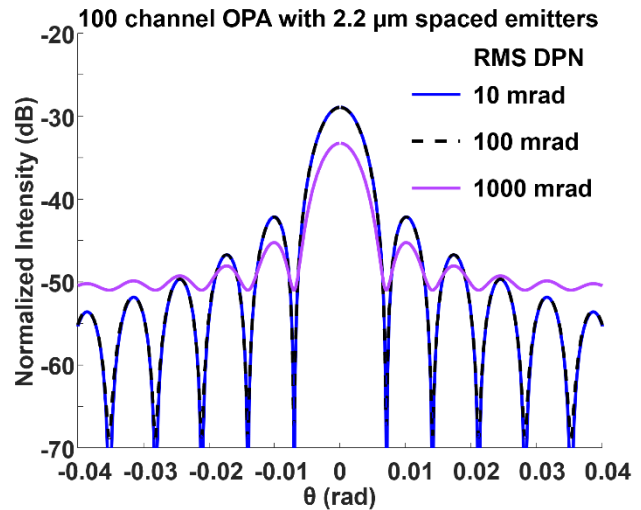


Fig. 6. Impact of RMS differential phase noise on far-field for a 100-channel OPA with emitters spaced $2.2 \mu\text{m}$ apart.

The impact of the DPN on the far-field beam pattern and the pointing error is evaluated through closed-form analytic equations for the case of emitters with uncorrelated phase errors between the elements [11] using equations (14-16). Additional effects resulting from the non-ideal behavior of the implemented OPA are not being considered here.

$$I_G^{\text{unpert}} = \frac{\sin^2(\pi N \theta d / \lambda)}{\sin^2(\pi \theta d / \lambda)} \quad (14)$$

$$I_G^{\text{uncorr}} = \exp(-\sigma_\phi^2) I_G^{\text{unpert}} + N(1 - \exp(-\sigma_\phi^2)) \quad (15)$$

$$\theta_{\text{pointingRMS}} = \frac{1}{2\pi} \sqrt{\frac{12\sigma_\phi^2}{N(N^2-1)d^2}} \quad (16)$$

Here, N is the number of channels in the array, θ is the angular position, d is the channel spacing, λ is the wavelength, σ_ϕ is the standard deviation of the phase error between two elements (RMS DPN), I_G^{unpert} is the unperturbed (ideal) far-field intensity, I_G^{uncorr} is the far-field intensity with uncorrelated phase errors, and $\theta_{\text{pointingRMS}}$ is the RMS pointing error.

Fig. 6 shows the influence of the RMS DPN on the far-field intensity for the case of a 100 element OPA with $2.2 \mu\text{m}$ channel spacing. The far-field patterns for the cases of 10 mrad and 100 mrad RMS DPN are close with differences visible at nulls. The side-lobe suppression ratio deteriorates by over 1 dB when the RMS DPN increases from 100 mrad to 1000 mrad. In comparison to the other cases, the degradation in the extinction ratio can be clearly seen for the case of 1000 mrad DPN, along with ~ 4 dB of reduction in the peak power of the main lobe.

Fig. 7 shows the calculated pointing error as a function of the number of array elements. The influence of the pointing error scales with the distance to the target. The RMS offset error of the beam from the desired location can be approximated as (distance \times RMS pointing error in rad). At a range of 100 m, RMS pointing errors in the range of $0.1 \mu\text{rad}$ to $100 \mu\text{rad}$ (RMS

> REPLACE THIS LINE WITH YOUR MANUSCRIPT ID NUMBER (DOUBLE-CLICK HERE TO EDIT) <

DPN=10 mrad) would result in the beam being off the target with RMS offset errors of 0.01 mm to 10 mm. For the case of 100 mrad DPN, the pointing errors in the range of 1 μ rad to 1000 μ rad deviates the beam by RMS offset errors of 0.1 mm to 100 mm. These pointing errors are less than the requirements for LiDAR applications in autonomous vehicles where the angular resolutions of up to 0.1° (1.7 mrad) [33] are needed. For short-range FSO (100 m in this case), in the case of 10 mrad DPN, these pointing errors do not result in the beam missing the aperture for receiver apertures of a few centimeters in size (RMS beam offset error ≤ 1 cm). The requirement on the receiver aperture increases to few tens of centimeters for the case of 100 mrad DPN (RMS beam offset error ≤ 10 cm).

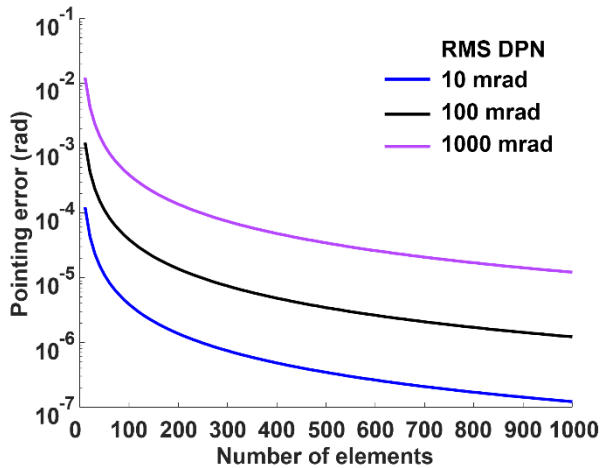


Fig. 7. Pointing error dependence on the number of elements and RMS differential phase noise.

The spectrum analyzer method of phase noise measurement does not reject the amplitude noise of the carrier. As a result, the real DPN values are lower than the measured DPN, which is considered an upper bound. A more accurate measurement of the DPN can be obtained by the interferometric method with correlation [34]. In the present case, the measured DPN is inherently low, has negligible impact on the far-field pattern, and results in pointing errors lower than the angular resolution requirements of LiDAR. Hence, more accurate measurement methods are not considered in the present case.

In the present case, the maximum value of the measured output optical power per channel is around -7 dBm (0.2 mW). The total output power (coherent beam combination of channels) scales with the number of channels. Hence, theoretically, the output power requirement for the application can be met by increasing the number of channels on the chip. Practically, the heat generated from the large number of amplifying channels could impact system performance and, consequently, the maximum output power and is the subject of a future investigation. Modeling the detailed effects of the SOA and the temporal path length fluctuations on DPN would improve the understanding of the system and is beyond the scope of the current work.

CONCLUSION

Inherently low RMS differential phase noise (<10 mrad) between the InP OPA channels is demonstrated across the C-band ($J_{\text{BSOA}}=J_{\text{chSOA}}=5$ kA/cm²). The inherently low DPN renders the amplifying, integrated OPA platform suitable for LiDAR and short-range FSO (100 m) without active phase locking. The results are promising for reducing the complexity of amplifying OPAs while maintaining low pointing error and minimally distorting the far-field pattern.

ACKNOWLEDGMENT

The authors would like to acknowledge Gilles Feugnet and Jerome Bourderionnet from Thales Research and Technology, for insightful technical discussions. Parts of this work have been presented at the 24th European Conference on Integrated Optics, 2023 [35] and IEEE Benelux Symposium 2022 [36].

REFERENCES

- [1] M. J. R. Heck, "Highly integrated optical phased arrays: Photonic integrated circuits for optical beam shaping and beam steering," *Nanophotonics*, vol. 6, no. 1, pp. 93–107, Jan. 2017, doi: 10.1515/nanoph-2015-0152.
- [2] P. F. McManamon et al., "Optical phased array technology," *Proceedings of the IEEE*, vol. 84, no. 2, pp. 268–298, 1996, doi: 10.1109/5.482231.
- [3] C.-P. Hsu et al., "A Review and Perspective on Optical Phased Array for Automotive LiDAR," *IEEE Journal of Selected Topics in Quantum Electronics*, vol. 27, no. 1, pp. 1–16, Jan.-Feb.2021, doi: 10.1109/JSTQE.2020.3022948.
- [4] J. He, T. Dong, and Y. Xu, "Review of photonic integrated optical phased arrays for space optical communication," *IEEE Access*, vol. 8, pp. 188284–188298, 2020, doi: 10.1109/ACCESS.2020.3030627.
- [5] W. M. Neubert, K. H. Kudielka, W. R. Leeb, and A. L. Scholtz, "Experimental demonstration of an optical phased array antenna for laser space communications," *Applied Optics*, vol. 33, no. 18, pp. 3820–3830, Jun. 1994, doi: 10.1364/AO.33.003820.
- [6] Y. Li and J. Ibanez-Guzman, "Lidar for Autonomous Driving: The Principles, Challenges, and Trends for Automotive Lidar and Perception Systems," *IEEE Signal Processing Magazine*, vol. 37, no. 4, pp. 50–61, Jul. 2020, doi: 10.1109/MSP.2020.2973615.
- [7] W. Xie, T. Komljenovic, J. Huang, M. Tran, M. Davenport, A. Torres, P. Pintus, and J. Bowers, "Heterogeneous silicon photonics sensing for autonomous cars [Invited]," *Optics Express*, vol. 27, no. 3, pp. 3642–3663, Feb. 2019, doi: 10.1364/OE.27.003642.
- [8] L. E. Roberts, R. L. Ward, C. Smith, and D. A. Shaddock, "Coherent Beam Combining Using an Internally Sensed Optical Phased Array of Frequency-Offset Phase Locked Lasers," *Photonics*, vol. 7, no. 4, p. 118, Nov. 2020, doi: 10.3390/photonics7040118.
- [9] L. E. Roberts et al., "Coherent beam combining using a 2D internally sensed optical phased array," *Applied Optics*, vol. 53, no. 22, pp. 4881–4885, Aug. 2014, doi: 10.1364/AO.53.004881.
- [10] J. H. Abeles and R. J. Deri, "Suppression of sidelobes in the far-field radiation patterns of optical waveguide arrays," *Appl Phys Lett*, vol. 53, no. 15, pp. 1375–1377, Oct. 1988, doi: 10.1063/1.99983.
- [11] C. D. Nabors, "Effects of phase errors on coherent emitter arrays," *Applied Optics*, vol. 33, no. 12, pp. 2284–2289, Apr. 1994, doi: 10.1364/AO.33.002284.
- [12] W. Liang et al., "Coherent beam combining with multilevel optical phase-locked loops," *JOSA B*, vol. 24, no. 12, pp. 2930–2939, Dec. 2007, doi: 10.1364/JOSAB.24.002930.
- [13] V. Jolivet et al., "Beam shaping of single-mode and multimode fiber amplifier arrays for propagation through atmospheric turbulence," *IEEE Journal of Selected Topics in Quantum Electronics*, vol. 15, no. 2, pp. 257–268, Mar. 2009, doi: 10.1109/JSTQE.2009.2011141.
- [14] K. Kikuchi, C. -E. Zah, and T. -P. Lee, "Measurement and analysis of phase noise generated from semiconductor optical amplifiers," *IEEE J Quantum Electronics*, vol. 27, no. 3, pp. 416–422, Mar.1991, doi: 10.1109/3.81340.
- [15] S. Ristic, A. Bhardwaj, M. J. Rodwell, L. A. Coldren, and L. A. Johansson, "An optical phase-locked loop photonic integrated circuit," *Journal of Lightwave Technology*, vol. 28, no. 4, pp. 526–538, Feb.2010, doi:10.1109/JLT.2009.2030341.

> REPLACE THIS LINE WITH YOUR MANUSCRIPT ID NUMBER (DOUBLE-CLICK HERE TO EDIT) <

[16] K. Balakier, M. J. Fice, L. Ponnampalam, A. J. Seeds, and C. C. Renaud, "Monolithically Integrated Optical Phase Lock Loop for Microwave Photonics," *Journal of Lightwave Technology*, vol. 32, no. 20, pp. 3893–3900, Oct. 2014, doi: 10.1109/JLT.2014.2317941.

[17] Y. Guo, Y. Guo, C. Li, H. Zhang, X. Zhou, and L. Zhang, "Integrated Optical Phased Arrays for Beam Forming and Steering," *Applied Sciences*, vol. 11, no. 9, p. 4017, Apr. 2021, doi: 10.3390/app11094017.

[18] K. Van Acoleyen, W. Bogaerts, and R. Baets, "Two-Dimensional Dispersive Off-Chip Beam Scanner Fabricated on Silicon-On-Insulator," *IEEE Photonics Technology Letters*, vol. 23, no. 17, pp. 1270–1272, 2011, doi: 10.1109/LPT.2011.2159785.

[19] J. Sun, E. Timurdogan, A. Yaacobi, E. S. Hosseini, and M. R. Watts, "Large-scale nanophotonic phased array," *Nature*, vol. 493, no. 7431, pp. 195–199, Jan. 2013, doi: 10.1038/nature11727.

[20] K. Komatsu, Y. Kohno, Y. Nakano, and T. Tanemura, "Large-Scale Monolithic InP-Based Optical Phased Array," *IEEE Photonics Technology Letters*, vol. 33, no. 20, pp. 1123–1126, Oct. 2021, doi: 10.1109/LPT.2021.3107277.

[21] M. Gagino, M. B. J. Van Rijn, E. A. J. M. Bente, M. K. Smit, and V. Dolores-Calzadilla, "Broadband Operation of an InP Optical Phased Array," *IEEE Photonics Technology Letters*, vol. 34, no. 10, pp. 541–544, May 2022, doi: 10.1109/LPT.2022.3171979.

[22] N. A. Tyler et al., "SiN integrated optical phased arrays for two-dimensional beam steering at a single near-infrared wavelength," *Optics Express*, vol. 27, no. 4, pp. 5851–5858, Feb. 2019, doi: 10.1364/OE.27.005851.

[23] C. V. Poulton et al., "Large-scale silicon nitride nanophotonic phased arrays at infrared and visible wavelengths," *Optics Letters*, vol. 42, no. 1, pp. 21–24, Jan. 2017, doi: 10.1364/OL.42.000021.

[24] L. M. Augustin et al., "InP-Based Generic Foundry Platform for Photonic Integrated Circuits," *IEEE Journal of Selected Topics in Quantum Electronics*, vol. 24, no. 1, Jan. 2018, doi: 10.1109/JSTQE.2017.2720967.

[25] M. Smit et al., "An introduction to InP-based generic integration technology," *Semicond Sci Technol*, vol. 29, no. 8, p. 083001, Jun. 2014, doi: 10.1088/0268-1242/29/8/083001.

[26] M. Smit, K. Williams, and J. Van Der Tol, "Past, present, and future of InP-based photonic integration," *APL Photonics*, vol. 4, no. 5, p. 050901, May 2019, doi: 10.1063/1.5087862.

[27] D. R. Gozzard, L. E. Roberts, J. T. Spollard, P. G. Sibley, and D. A. Shaddock, "Fast beam steering with an optical phased array," *Opt Lett*, vol. 45, no. 13, pp. 3793–3796, Jul. 2020, doi: 10.1364/OL.393007.

[28] K. Yang et al., "Coherent Polarization Beam Combination by Microcontroller-Based Phase-Locking Method," *IEEE Photonics Technology Letters*, vol. 28, no. 20, pp. 2129–2132, Oct. 2016, doi: 10.1109/LPT.2016.2582500.

[29] M. Prost et al., "Optical phased array with on-chip phase calibration," *Opt Lett*, vol. 47, no. 23, 2022, doi: 10.1364/OL.467779.

[30] F. Lemaitre, S. Kleijn, A. J. Millan-Mejia, K. Williams, and V. Dolores-Calzadilla, "High Density Integration of Semiconductor Optical Amplifiers in InP Generic Photonic Integration Technology," *IEEE Journal of Selected Topics in Quantum Electronics*, vol. 28, no. 6, Nov.-Dec 2022, doi: 10.1109/JSTQE.2022.3210663.

[31] N. Kuse and M. E. Fermann, "Electro-optic comb based real time ultra-high sensitivity phase noise measurement system for high frequency microwaves," *Scientific Reports*, vol. 7, no. 1, p. 2847, Jun. 2017, doi: 10.1038/s41598-017-03049-5.

[32] A. H. Nguyen, J. H. Cho, H. J. Bae, and H. K. Sung, "Side-lobe Level Reduction of an Optical Phased Array Using Amplitude and Phase Modulation of Array Elements Based on Optically Injection-Locked Semiconductor Lasers," *Photonics*, vol. 7, no. 1, p. 20, Feb. 2020, doi: 10.3390/photonics7010020.

[33] Z. Dai, A. Wolf, P. P. Ley, T. Glück, M. C. Sundermeier, and R. Lachmayer, "Requirements for Automotive LiDAR Systems," *Sensors* vol. 22, no. 19, p. 7532, Oct. 2022, doi: 10.3390/s22197532.

[34] E. Rubiola and V. Giordano, "Phase Noise Metrology," In: Planat, M. (eds) *Noise, Oscillators and Algebraic Randomness. Lecture Notes in Physics*, vol 550. Springer, Berlin, Heidelberg., pp. 189–215, Aug. 2000, doi: 10.1007/3-540-45463-2_10.

[35] B. S. Vikram, M. Gagino, A. Millan-Mejia, L. Augustin, K. A. Williams, and V. Dolores Calzadilla, "Demonstration of low RMS differential phase noise across C-band for integrated, amplifying optical phased arrays," in 24th European Conference on Integrated Optics, Th 2.10, pp. 72–74, 2023.

[36] B. S. Vikram, M. Gagino, A. Millan-Mejia, L. Augustin, K. A. Williams, and V. Dolores Calzadilla, "Demonstration of low differential phase noise for optical phased arrays with optical amplification," in Proceedings of the 26th

Annual Symposium of the IEEE Photonics Benelux Chapter, 2022. [Online]. Available: https://photonics-benelux.org/wp-content/uploads/pb-files/proceedings/2022/Posters/Poster_46.pdf



B.S. Vikram (Member, IEEE) received the M.Tech degree in Integrated Circuit Technology from the University of Hyderabad, Hyderabad, India with a thesis on "Voltage Tunable Phase Shifters using Paraelectric BST Varactors" in 2015 and the Ph.D. degree from the Indian Institute of Science, Bangalore, India with a thesis on "Architectures for Enhancing Bandwidth and Power Scalability of Optical Frequency Combs" in 2021. From 2021, he is working as a postdoctoral researcher at the Eindhoven University of Technology. He is currently working on FMCW LiDAR systems. His other areas of interest include systems for frequency combs, nonlinear fiber optics, and electro-optic modulation.

Marco Gagino, received the B.Sc. in Engineering Physics from the Politecnico di Torino, Italy, and the M.Sc in Micro and Nanotechnologies for Integrated Systems from the Politecnico di Torino, Italy and the Grenoble INP, France. Since 2020, he is a Ph.D. candidate at the Eindhoven University of Technology working on the InP photonic integration of optical phased arrays for LiDAR.

A.Millan-Mejia. (Member, IEEE), received the B.Eng. in Telecommunications with honours from the National Autonomous University of Mexico, the degree in M.Sc. Applied Physics from the Delft University of Technology, Delft, the Netherlands and the M. Eng. Photonics from the Warsaw University of Technology, Warsaw, Poland. In 2018, he obtained his PhD degree from the Eindhoven University of Technology, the Netherlands, from his work on InP membrane on a silicon platform, focusing on developing high-speed modulators. As a Senior Scientist at SMART Photonics, he is involved in developing new integration fabrication technologies and new building blocks for the photonics integration generic platform.

L. Augustin (M'99) received the M.Sc. and Ph.D. degrees in electrical engineering from the Eindhoven University of Technology, Eindhoven, The Netherlands. He was a Process Engineer in Cedova, which later became Photonics Laboratory as a part of Philips Research. After this, he switched to Photovoltaics and was a Senior R&D Engineer in Solland Solar. In 2012, he was a Project Manager at Eindhoven University and joined SMART Photonics B.V. Since 2014, he has been a CTO at SMART Photonics, Eindhoven, The Netherlands. His expertise is in simulation and design of InP-based photonic integrated circuits, fabrication of III-V photonics components and integrated circuits, and characterization of semiconductor-based photonic components.

K.A. Williams (Member, IEEE), received the B.Eng. degree from the University of Sheffield, Sheffield, U.K., and the Ph.D. degree from the University of Bath, Bath, U.K., in

> REPLACE THIS LINE WITH YOUR MANUSCRIPT ID NUMBER (DOUBLE-CLICK HERE TO EDIT) <

1995. He moved to the University of Cambridge, Cambridge, U.K., in 2001 and was elected Fellow at Churchill College. His research interests are in the area of integrated photonic circuits. He was the recipient of a Royal Society University research fellowship at the University of Bristol, Bristol, U.K., in 1996. In 2006, he was the recipient of a European Commission Marie Curie Chair at the COBRA Institute, now known as the Institute for Photonic Integration at the Eindhoven University of Technology, The Netherlands. In 2011, he was the recipient of a Vici award from the Netherlands Organization for Scientific Research, where he has focused on photonic integration technology. He is the chair of the Photonic Integration research group at Eindhoven University of Technology.



V. Dolores Calzadilla received the B.Eng. in Telecommunications with honors from the National Autonomous University of Mexico, and the degree in M.Sc. Photonics from the Friedrich Schiller University Jena, Germany, with a thesis on optical metrology at Carl Zeiss. In 2016, he obtained the Ph.D. degree (cum laude) from the Eindhoven University of Technology, the Netherlands, and then became a scientist at the Fraunhofer Heinrich Hertz Institute, Berlin, Germany, within the Department of Photonic Components. Since 2018, he is with the Eindhoven University of Technology (TU/e). He is an Assistant Professor at TU/e and a Program Manager at the Photonic Integration Technology Centre (PITC). He has a strong expertise in III-V photonic integrated circuits (PIC) technology, both on generic and membrane-based platforms, and is currently engaged in PIC-based sensing research as well as technology development in cooperation with industry.